

Ground-state phases of $S = 1/2$ Heisenberg models on the body-centered cubic lattice

Rajah P. Nutakki^{1,2} and Filippo Vicentini^{1,2}

¹*CPHT, LIX, CNRS, Inria, École Polytechnique,*

Institut Polytechnique de Paris, 91120 Palaiseau, France.

²*Collège de France, Université PSL, 11 place Marcelin Berthelot, 75005 Paris, France*

Simulating low-temperature properties of three-dimensional frustrated quantum magnets is challenging due to the sign problem and the system sizes required to mitigate substantial finite-size effects. However, there are many experimental examples of three-dimensional crystals that could host exotic low-temperature states of matter, such as quantum spin liquids. We calculate the ground-state phase diagrams of frustrated quantum spin models on the body-centered cubic lattice using neural quantum states. First, we study the antiferromagnetic $J_1 - J_2$ model where we find a direct first-order phase transition between Néel and collinear long-range-ordered phases at $(J_2/J_1)_c = 0.705$, consistent with previous studies. Then, in a tetragonally-distorted variant, proposed as a minimal model of $\text{NaCa}_2\text{Cu}_2(\text{VO}_4)_3$, we find no evidence of a quantum paramagnetic ground state, with a first-order phase transition between Néel and chain phases at $(J_{2ab}/J_1)_c = 1.0375$. Therefore, the ground state of the tetragonally-distorted model does not reproduce the low-temperature magnetic properties of $\text{NaCa}_2\text{Cu}_2(\text{VO}_4)_3$, and the inclusion of other effects is necessary to rationalize experimental observations.

I. INTRODUCTION

Finding new states of matter in solid-state materials is an important challenge, both fundamentally, in terms of understanding what phases of matter are possible and from a practical point of view for developing new technologies. In frustrated magnetism [1], a key goal has been to positively identify quantum spin liquids (QSLs). In three-dimensional crystals, there are several candidate systems [2–6], notably the rare-earth pyrochlores [7–15], displaying signatures of spin-fractionalization and emergent gauge fields. Recent experimental work [16, 17] on vanadate garnets [18, 19], in particular the absence of magnetic order, dynamic Cu^{2+} moments down to 50 mK and broad, dispersive features in the dynamical structure factor in $\text{NaCa}_2\text{Cu}_2(\text{VO}_4)_3$ (NCCVO) [17] suggests spin models on the body-centered cubic lattice with competing exchange interactions could host QSL physics.

Identifying QSLs in solid-state materials requires accurate numerical simulations to identify specific signatures of the proposed QSL that can be compared to experiments. However, accurately simulating the low-temperature properties of three-dimensional frustrated quantum magnets is a significant challenge in itself, due to the sign problem and the large number of variables that must be simulated to mitigate finite-size effects. Methods that have been successfully applied include diagrammatic techniques: pseudo-(Majorana)fermion functional renormalization group (PFFRG) [20–24] and diagrammatic Monte Carlo [25–27], variational approaches: DMRG [28], many-variable variational Monte Carlo [29–31], and cluster methods [32, 33]. These methods face distinct challenges, such as reaching low temperatures in the diagrammatic case, entanglement truncation for DMRG or physical bias in the ansatz for many-variable variational Monte Carlo.

Recently, advances in the use of neural networks as physically unbiased variational ansatze (neural quantum

states) have obtained high-accuracy ground states for two-dimensional frustrated quantum magnets [34–38]. This approach can, in principle, be extended to three-dimensional systems, however, there are few examples in the literature [30].

In this work, we apply neural quantum states (NQS) to study the ground states of frustrated $S = 1/2$ Heisenberg models on the body-centered cubic lattice, simulating lattices of up to 288 spins. First, we study the (cubic-symmetric) antiferromagnetic $J_1 - J_2$ model,

$$\hat{H}_{\text{cub}} = J_1 \sum_{\langle ij \rangle} \hat{\mathbf{S}}_i \cdot \hat{\mathbf{S}}_j + J_2 \sum_{\langle\langle ij \rangle\rangle} \hat{\mathbf{S}}_i \cdot \hat{\mathbf{S}}_j, \quad (1)$$

where J_1 (J_2) couples first (second) nearest neighbors, as illustrated in Fig. 1. Our large-scale variational calculations find a first-order phase transition between long-range-ordered Néel and collinear phases at $(J_2/J_1)_c = 0.705 \pm 0.005$, slightly higher than the location of the phase transition in the corresponding classical Ising model at $(J_2/J_1)_c = 0.67$, and consistent with previous results [39–44].

We then turn to an experimentally relevant tetragonally-symmetric variant,

$$\hat{H}_{\text{tet}} = J_1 \sum_{\langle ij \rangle} \hat{\mathbf{S}}_i \cdot \hat{\mathbf{S}}_j + J_{2c} \sum_{\langle ij \rangle \in 2c} \hat{\mathbf{S}}_i \cdot \hat{\mathbf{S}}_j + J_{2ab} \sum_{\langle ij \rangle \in 2ab} \hat{\mathbf{S}}_i \cdot \hat{\mathbf{S}}_j, \quad (2)$$

where the J_2 term is split into couplings along the z (J_{2c}), and x, y -directions (J_{2ab}), see Fig. 1c. This was proposed as a minimal model of the low-temperature magnetic properties of NCCVO with $J_1 = 1$, $J_{2c} = -4.9$ and $J_{2ab} = 1.7$ [17].

In a classical Ising model of Eq. 2, with J_{2c} ferromagnetic and J_1, J_{2ab} antiferromagnetic, one expects a phase transition between Néel and chain phases at $J_{2ab}/J_1 = 1$. An intermediate quantum spin liquid phase between these phases in the quantum model would provide a qualitative explanation for the low-temperature

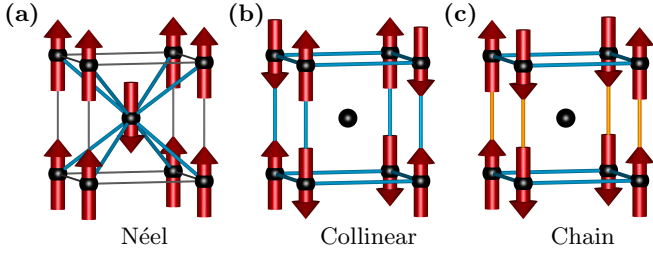


FIG. 1. Ground states of the classical cubic and tetragonal $J_1 - J_2$ models on the body-centered cubic lattice. The exchange interactions satisfied by the state are highlighted. (a) Antiferromagnetic J_1 interactions are satisfied in the Néel state, (b) antiferromagnetic J_2 interactions by the collinear state and (c) antiferromagnetic J_{2ab} (blue), ferromagnetic J_{2c} (yellow) by the chain state. The sites shown make up the two-site cubic unit-cell of the body-centered cubic lattice.

experimental measurements on NCCVO. We study the ground-state phase diagram of this model for $J_1 = 1$, $J_{2c} = -4.9$ and varied J_{2ab} to investigate this possibility.

We do not find evidence for a quantum paramagnetic ground state, only finding long-range-ordered Néel and chain states in the parameter regime studied, with a first-order phase transition between the two at $J_{ab} = 1.0375 \pm 0.0125$. This suggests the model is missing a key feature to describe the low-temperature properties of NCCVO, possibly the effect of further neighbor couplings [44]. Furthermore, our work demonstrates how NQS can be used to study the low-energy properties of frustrated three-dimensional quantum Hamiltonians with hundreds of spins, assisting in the interpretation of experimental observations by providing ground-state phase diagrams of relevant minimal models.

II. METHOD

We use variational Monte Carlo with a factored vision transformer [45] wavefunction adapted to three-dimensional systems. The network hyperparameters are: depth 4, feature dimension 64, 8 heads and a factored-attention that spans all patches, giving a total parameter count of $\sim 10^5$ parameters. The wavefunction is, by construction, projected to a specific momentum \mathbf{k} following the approach discussed in Ref. [46]. Point group symmetries are enforced by quantum number projection [29, 47, 48], such that the wavefunction is symmetrized to an irreducible representation (irrep) of the lattice space group. We restrict the calculation to the $\sum_i S_i^z = 0$ sector by a magnetization-conserving sampling scheme. We simulate periodic (L_x, L_y, L_z) clusters of the cubic, two-site, unit cell, with lattice constant $a = 1$ (Fig. 1), and minSR [35, 36] to optimize the variational wavefunction.

To elucidate ground-state properties of the optimized

wavefunctions, we compute the static structure factor

$$S(\mathbf{q}) = \frac{1}{N} \sum_{i,j} e^{i\mathbf{q} \cdot (\mathbf{r}_i - \mathbf{r}_j)} \langle \hat{\mathbf{S}}_i \cdot \hat{\mathbf{S}}_j \rangle \quad (3)$$

and associated correlation ratios [49–51],

$$R(\mathbf{Q}) = 1 - \frac{S(\mathbf{Q} + \delta\mathbf{q})}{S(\mathbf{Q})}, \quad (4)$$

where

$$\begin{aligned} \mathbf{Q}_{\text{Néel}} &= (2\pi, 2\pi, 2\pi), \\ \mathbf{Q}_{\text{Collinear}} &= (\pi, \pi, \pi), \\ \mathbf{Q}_{\text{Chain}} &= (\pi, \pi, 0), \end{aligned} \quad (5)$$

are the ordering wavevectors of the respective ordered states (see Fig. 1), \mathbf{r}_i the position of the lattice site i , $\delta\mathbf{q} = (2\pi/L_x, 0, 0)$ (a minimum step in momentum space), and the expectation value $\langle \dots \rangle$ is estimated from Monte Carlo sampling of the optimized wavefunction. The correlation ratio allows us to diagnose whether the ground state is an ordered or disordered phase in the thermodynamic limit. It increases with system size in a magnetically-ordered phase and decreases in a magnetically-disordered phase.

III. RESULTS AND DISCUSSION

A. Cubic Model

First, we study the ground-state phase diagram of the cubic $J_1 - J_2$ model. To benchmark the method we compute the variational energies of our optimized wavefunction for a $N = 32$, $(L_x, L_y, L_z) = (4, 2, 2)$ lattice. As shown in Fig. 2, the relative errors against the exact ground-state energy computed by exact diagonalization are $\lesssim 10^{-4}$ for all values of J_2 . We also perform calculations for $N = 64(4, 4, 2)$, $N = 128(4, 4, 4)$ and $N = 288(6, 6, 4)$ lattices. For all system sizes and phases of the model we find that the ground state is in the $\mathbf{k} = (0, 0, 0)$, trivial point group irrep of the space group (see Appendix A).

Results for the ground-state energy and correlation ratios are presented in Fig. 2. The energy is linear on both sides of the critical point, J_2^c , with the resulting discontinuity in $\frac{\partial E}{\partial J_2}|_{J_2^c}$ characteristic of a first-order phase transition. Similarly, $R(\mathbf{Q})$ is discontinuous at J_2^c and increases with system size within the respective phases, indicating a long-range-ordered phase in the thermodynamic limit. Therefore, in agreement with previous studies [39–44], we find a direct first-order transition between the ordered ground states of the cubic $J_1 - J_2$ model.

For system sizes with minimum side length, $L_{\min} = 2$, we observe a significant size-dependence of J_2^c , in contrast to the exact diagonalization study of Ref. [39], where the observed system size dependence is small. This is

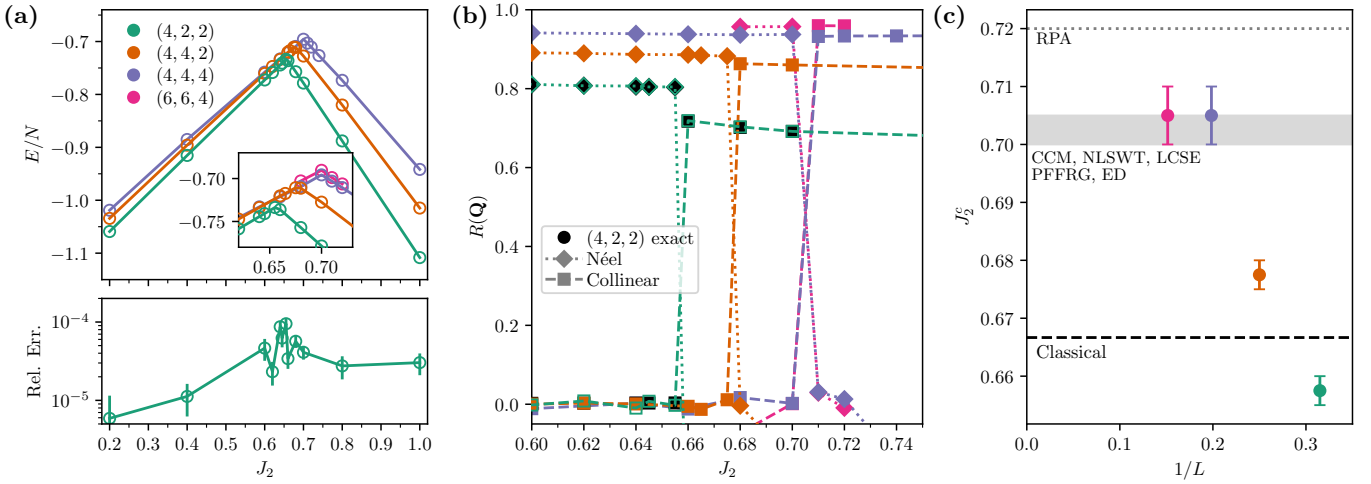


FIG. 2. (a) (Top) Variational energy per site for the cubic-symmetric model. (Bottom) Relative error of variational energies compared to exact diagonalization for the $(4, 2, 2)$ lattice. Error bars (smaller than point size in the top panel) are the Monte Carlo errors when computing expectation values from the optimized wavefunction. (b) Correlation ratios for Néel and collinear orders, showing a first-order transition between the two with a critical point, J_2^c , that has a strong system size dependence for lattices with minimum side length 2. The correlation ratios increase with system size in the respective phases, indicating a long-range-ordered phase in the thermodynamic limit. Exact values computed from exact diagonalization are shown. (c) The change in J_2^c with system size where $L = N^{1/3}$. Error bars are given by the spacing of J_2 points for which we obtain converged variational solutions. Our values of J_2^c for system sizes with a minimum side length of 4 are consistent with values in the literature obtained via other methods [39–41, 43, 44] (gray band), which are well-approximated by the RPA value [42].

likely because for the lattices we use with a side length of 2 and periodic boundaries, J_2 bonds couple the same sites twice along the short directions. Nevertheless for $L_{\min} = 4$, we do not find any significant system size dependence of J_2^c , suggesting that $L_{\min} \geq 4$ is required on this lattice to be free of severe finite-size effects. For these system sizes we find $J_2^c = 0.705 \pm 0.005$, consistent with results from exact diagonalization (ED) [39], coupled-cluster method (CCM) [43], non-linear spin wave theory (NLSWT) [41], linked cluster series expansions (LCSE) [40] and PFFRG [44].

Our variational calculation is correctly able to capture the ground-state physics, even around J_2^c where the sign problem is most severe (both in terms of quantum Monte Carlo and complexity of the ground-state sign structure [39] (see Appendix C) on lattices of up to 288 spins. Therefore in the following section we apply our variational approach to the tetragonally-distorted $J_1 - J_2$ model, to investigate the possibility of a quantum paramagnetic ground state.

B. Tetragonal Model

Variational results for the tetragonal $J_1 - J_2$ model with $J_1 = 1, J_{2c} = -4.9$ and varied J_{2ab} are shown in Fig. 3. As for the cubic model, relative errors for the $(4, 2, 2)$ lattice are $< 10^{-4}$ for all J_{2ab} , and we find that the ground state is in the $\mathbf{k} = (0, 0, 0)$, trivial point group irrep (see Appendix A). Given the finite-size effects

observed in the cubic model for $L_{\min} \leq 2$ we also perform calculations for $N = 128(4, 4, 4)$, $N = 256(8, 4, 4)$ and $N = 288(6, 6, 4)$ lattices. We find a direct first-order phase transition between the Néel and chain long-range-ordered phases, with a discontinuity in $R(\mathbf{Q})$ and $\frac{\partial E}{\partial J_{2ab}}|_{J_{2ab}^c}$ at the transition point, J_{2ab}^c . We find a small system size dependence of J_{2ab}^c , increasing by 1.25×10^{-2} from the $(4, 4, 4)$ to $(8, 4, 4)$ system, both consistent with the $(6, 6, 4)$ value of $J_{ab}^c = 1.0375 \pm 0.0125$, with error given by the resolution of our converged calculations. While the correlation ratio in the Néel phase decreases slightly going from the $(4, 4, 4)$ to $(8, 4, 4)$ lattice, this is likely due to the fact that we are halving $\delta\mathbf{q}$ whilst only increasing N by a factor of 2. Otherwise correlation ratios increase with system size in the respective ordered phases, indicative that these ordered phases survive in the thermodynamic limit. Therefore, we find that the tetragonal $J_1 - J_2$ model does not host a quantum paramagnetic ground state at the intersection of Néel and chain phases.

Previous work [44] found that a cubic-symmetric $J_1 - J_2 - J_3$ model will host a quantum paramagnetic phase [44], nearby in parameter space to the intersection of Néel, collinear and chain phases, where this phase competition can provide a larger low-energy manifold of states from which a quantum paramagnet can be stabilized by quantum fluctuations. The competition in the tetragonal $J_1 - J_2$ model (as in the cubic model) is only between two phases, which does not appear to be sufficient to stabilize a quantum paramagnet.

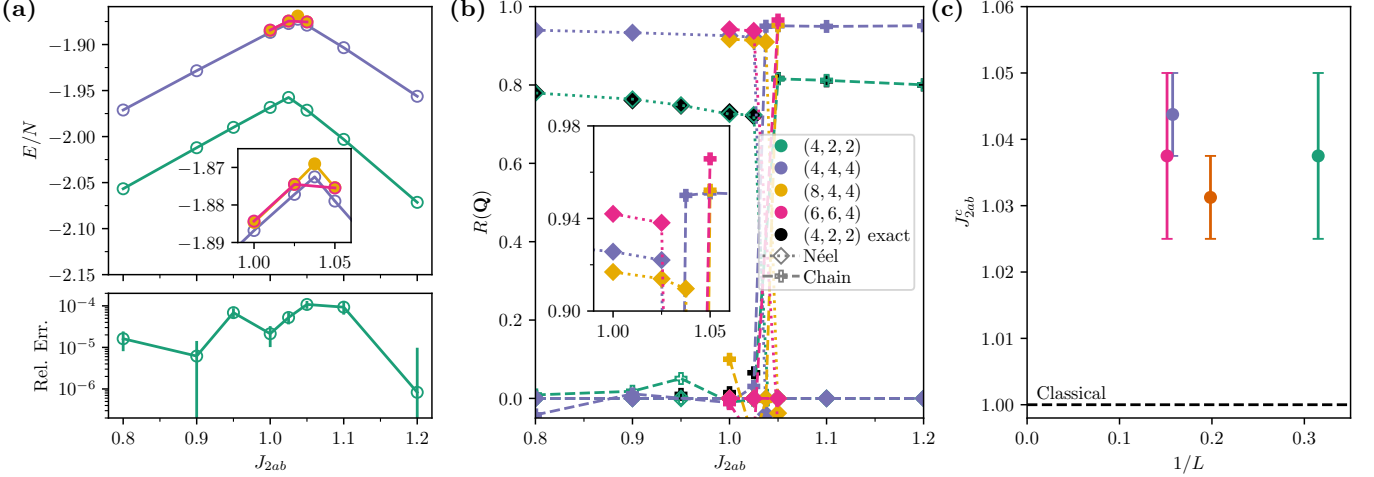


FIG. 3. (a) (Top) Variational energy per site for the tetragonal model. (Bottom) Relative error of variational energies compared to exact diagonalization for the $(4, 2, 2)$ lattice. Error bars are from Monte Carlo sampling of the optimized wavefunction. (b) Correlation ratios for the respective ordered phases, generally showing an increase with system size, indicative of long-range-ordered phases in the thermodynamic limit, and no significant shift in the critical point, J_{2ab}^c . Exact values from exact diagonalization are shown. (c) The change in J_{2ab}^c with system size where $L = N^{1/3}$. Error bars are given by the spacing of J_{2ab} points for which we obtain converged variational solutions. The values are consistent with $J_{2ab}^c = 1.0375 \pm 0.0125$, higher than $J_{2ab}^c = 1$ expected for the classical Ising model.

Adding J_3 terms with tetragonal symmetry to Eq. 2 with classical Ising spins, $s_i = \pm 1$, results in the following Hamiltonian

$$H = J_1 \sum_{\langle ij \rangle} s_i s_j + J_{2c} \sum_{(ij) \in 2c} s_i s_j + J_{2ab} \sum_{(ij) \in 2ab} s_i s_j + J_{3c} \sum_{(ij) \in 3c} s_i s_j + J_{3ab} \sum_{(ij) \in 3ab} s_i s_j, \quad (6)$$

where the J_{3c} term couples third neighbors with a displacement in the z -direction, J_{3ab} third neighbors with a displacement in the $x - y$ plane. An intersection of the three ordered phases exists at, for example, $J_1 = 1$, $J_{2c} = -5$, $J_{2ab} = 3.5$, $J_{3c} = -1.25$, any J_{3ab} . Therefore a ferromagnetic J_{3c} is one mechanism by which phase competition between the three phases could be introduced, a potential pathway to a quantum paramagnetic ground state.

Our results suggest that the tetragonal $J_1 - J_2$ at zero temperature is not the correct minimal model to describe the phenomena observed in experiments on NCCVO. Further neighbor interactions, finite temperature and chemical disorder of non-magnetic Na and Ca ions are all effects that may need to be included in order to capture the experimentally observed behavior.

IV. CONCLUSION AND OUTLOOK

We have applied NQS to study the ground-state phase diagrams of both cubic and tetragonally-symmetric $J_1 - J_2$ models on the body-centered cubic lattice. In the cubic $J_1 - J_2$ model we find a first-order phase transition

between Néel and collinear phases at $J_2^c = 0.705 \pm 0.005$, in agreement with previous studies. For the tetragonal model, recently proposed as a minimal model for the magnetic properties of NCCVO, where there is evidence for a dynamic, paramagnetic low-temperature state, we also find a first-order phase transition between Néel and chain phases at $J_{ab} = 1.0375$, with no evidence for a quantum paramagnetic phase. This suggests that other effects will need to be included to correctly model the experimentally-observed phenomena.

Since a quantum paramagnetic phase was previously found near the intersection of Néel, collinear and chain phases [44] we suggest that the inclusion of a ferromagnetic J_{3c} could induce a similar phase competition in the tetragonal $J_1 - J_2 - J_3$ model, so could host a quantum paramagnetic ground state. Future work could map out both classical and quantum ground-state phase diagrams of this model to investigate this possibility.

We have demonstrated how NQS can be used to study experimentally-relevant questions in three-dimensional frustrated magnets. Expanding this to geometrically (rather than exchange)-frustrated three-dimensional lattices, such as the pyrochlore, could require learning more complex ground-state sign structures [52, 53], which may not be easily done with current techniques. Understanding how to address this issue would be an important step to broaden the applicability of NQS to frustrated magnets.

DATA AND CODE AVAILABILITY

The data supporting the findings of this article are available [54], as well as the code for our NQS calculations [55].

ACKNOWLEDGMENTS

We thank F. Bert and K. Salou-Smith for useful discussions, and E. Kermarrec, F. Alet and S. Capponi for helpful discussions and comments on the manuscript. The authors acknowledge support by the French Agence Nationale de la Recherche through the NDQM project, grant ANR-23-CE30-0018. This work was performed using HPC resources from GENCI-IDRIS (Grants 2025-AD010517107 and 2024-A0170515698) on the V100 and A100 partitions of Jean-Zay.

Appendix A: Symmetry sectors

We use a wavefunction projected to a momentum sector, \mathbf{k} , of the patched lattice. Since we work with a simple-cubic Bravais lattice with patches made up of the two-site basis, the translation group is that of the simple-cubic lattice. The wavefunction can further be projected to space-group sectors through quantum number projection [29, 47, 48, 56] over the corresponding little group characters, χ_g , as well as to a spin-parity sector, via

$$\Psi_{\mathbf{k}, L_{\mathbf{k}}, \theta}(\sigma) = \frac{1}{|L_{\mathbf{k}}|} \sum_{g \in L} \chi_g \Psi_{\mathbf{k}, \theta}(g^{-1} \sigma) \quad (\text{A1})$$

and

$$\Psi_{\mathbf{k}, L_{\mathbf{k}}, P, \theta}(\sigma) = \frac{1}{2} (\Psi_{\mathbf{k}, L_{\mathbf{k}}, \theta}(\sigma) \pm_P \Psi_{\mathbf{k}, L_{\mathbf{k}}, \theta}(-\sigma)). \quad (\text{A2})$$

In practice, we gradually introduce symmetries during the course of the optimization [45].

In order to ascertain the symmetry sector of the ground state, we perform optimizations and projections in the various sectors for each system size up to and including $(4, 4, 4)$ at $J_2 = 0.2, 1$ of the cubic model and $J_{2ab} = 0.2, 1.5$ of the tetragonal model. First, we perform optimizations for all \mathbf{k} in the irreducible Brillouin zone. Then we project the wavefunction of the optimized solution to all corresponding little group sectors, giving us the space-group sector of the ground state. Finally, we project the optimal space-group symmetrized wavefunction to the two spin-parity sectors. As shown in Fig. 4, we find that this projection procedure gives the same optimal symmetry sector as performing further optimization of the wavefunction after projection. We find the optimal symmetry sector is always the $\mathbf{k} = (0, 0, 0)$, invariant little group irrep and spin-parity symmetric sector, although there is a quasi-degeneracy in the little group with other sectors for $J_2 = 1$ of the cubic model and $J_{ab} = 1.5$ of the tetragonal.

Appendix B: Patching

In order to compare the effects of different patchings in our variational wavefunction, we perform optimizations for the $(4, 2, 2)$ lattice using various patch shapes. We define patch shapes in units (n_x, n_y, n_z) of the cubic lattice vectors, comparing a $(1, 1, 1)$ patch (2 sites), $(2, 2, 1)$ patch (8 sites) and $(2, 2, 2)$ patch (16 sites). To ensure the results are comparable, we optimize first without enforcing any additional translational symmetries, before enforcing all intrapatch translations, resulting in a wavefunction that is invariant under the full translation group of the lattice. We compare the relative difference of the minimum energies obtained for each patch size,

$$\Delta = \frac{E - E_{\text{ref}}}{E_{\text{ref}}}, \quad (\text{B1})$$

where E_{ref} is the minimum energy obtained using patch shape $(1, 1, 1)$. A comparison across different values of J_2 is presented in Figure 5, which shows that there is no significant, systematic, difference in variational energies obtained using different patchings.

Appendix C: Sign Structure

The Marshall sign rules [57] (see the appendix of Ref. [58] for a concise explanation) that give the exact ground-state sign structure in various limits of the Hamiltonian are

$$s_{\mu}(\sigma) = (-1)^{n_{\uparrow, \mu}} \quad (\text{C1})$$

with $n_{\uparrow, \mu}$ the number of spins on the sublattice μ . The various sublattices are illustrated in Fig. 6.

For the cubic $J_1 - J_2$ model, we verify whether variational energies can be improved by explicitly accounting for the Marshall sign rules in the $J_1 = 0$ and $J_2 = 0$ limits by using the ansatz

$$\Psi_{\mu, \theta}(\sigma) = s_{\mu}(\sigma) \Psi_{\theta}(\sigma), \quad (\text{C2})$$

As shown in Figure 7a the explicit incorporation of a sign rule does not improve variational energies for the $(4, 2, 2)$ lattice, suggesting the network is able to easily learn these sign rules during the optimization.

To quantify the ground-state sign structures, we compute the expectation value of the Marshall-corrected sign of the optimized wavefunction

$$\langle \text{sign}_{\mu} \rangle = \sum_{\sigma} |\Psi_{\theta}(\sigma)|^2 s_{\mu}(\sigma) \text{sign}(\Psi_{\theta}(\sigma)). \quad (\text{C3})$$

A wavefunction whose ground-state sign structure is exactly given by a Marshall sign rule yields $\langle \text{sign}_{\mu} \rangle = 1$, whereas $\langle \text{sign}_{\mu} \rangle = 0$ means there is no correlation between the Marshall and actual sign of the wavefunction.

Results for $\langle \text{sign}_{\mu} \rangle$ for variational solutions of both cubic and tetragonal models are shown in Fig. 7b. In the cubic case, as observed in exact diagonalization [39], across

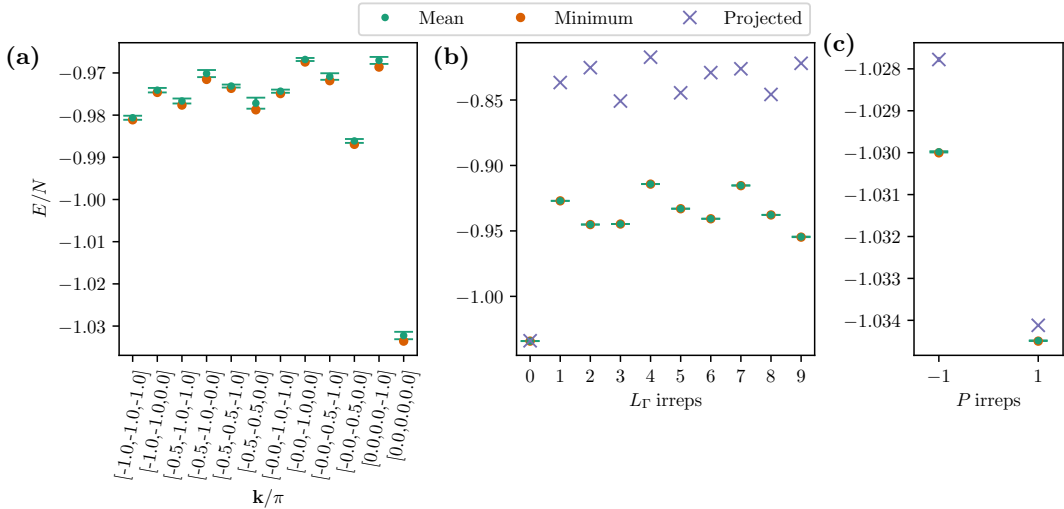


FIG. 4. Finding the optimal symmetry sector for the cubic model. (a-c) Variational energies obtained in different symmetry sectors for $(4, 4, 2)$, $J_2 = 0.2$. The mean is the final energy of 5 different runs with error bars given by the standard deviation. We also plot the energy obtained by projecting the wavefunction from the previous symmetry stage without any optimization. First, (a), optimizations are carried out for all momenta in the irreducible Brillouin zone. Then, (b), starting from the optimized states, further optimizations/projections are carried out for all irreps of the little group of $\mathbf{k} = \Gamma = (0, 0, 0)$, giving us the optimal space-group sector. Finally, (c), further optimizations/projections are carried out in the spin-parity antisymmetric/symmetric sectors. Since projections find the same optimal symmetry sector as running further optimizations, for $N \geq 128$ and all system sizes on the tetragonal model we only run optimizations for different momenta then project the optimized states to find the optimal symmetry sectors.

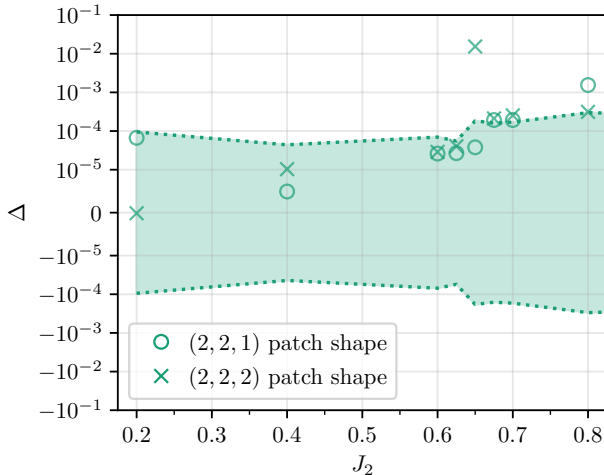


FIG. 5. Comparison of the relative difference of variational energies obtained using different patchings for the $(4, 2, 2)$ lattice, computed relative to a $(1, 1, 1)$ patch. The shaded regions correspond to the error, due to fluctuations during the final iterations of the optimization. There is no systematic difference between the patchings.

the entire Néel phase the Marshall-corrected sign is almost exactly 1, whereas in the collinear phase the sign increases with J_2 . As system size is increased the average sign at fixed J_2 in the collinear phase decreases. In the tetragonal case, the results are similar, but with a lower average sign in the large J_{2ab} phase. The minimum per-

centage of positive signs after Marshall sign correction we observe across all system sizes and parameters is 70%.

It is known that NQS struggles with complex sign structures [52, 53, 59], but that the ViT can learn Marshall sign rules [37], so the fact that Marshall sign rules give a reasonable percentage of the ground-state signs may be one factor in the success of our approach for the models we study.

Appendix D: Structure Factors and Correlation Ratios

Static structure factors (Eq. 3) for the ground states we obtain for the cubic and tetragonal models are shown in Fig. 8 and Fig. 9 respectively. As expected from the correlation ratios, the Bragg peaks of the respective ordered phases sharpen as system size is increased. We also plot the order parameters,

$$m^2(\mathbf{Q}) = \frac{S(\mathbf{Q})}{N} \quad (D1)$$

in Fig. 10, with values of \mathbf{Q} defined in Eq. 6.

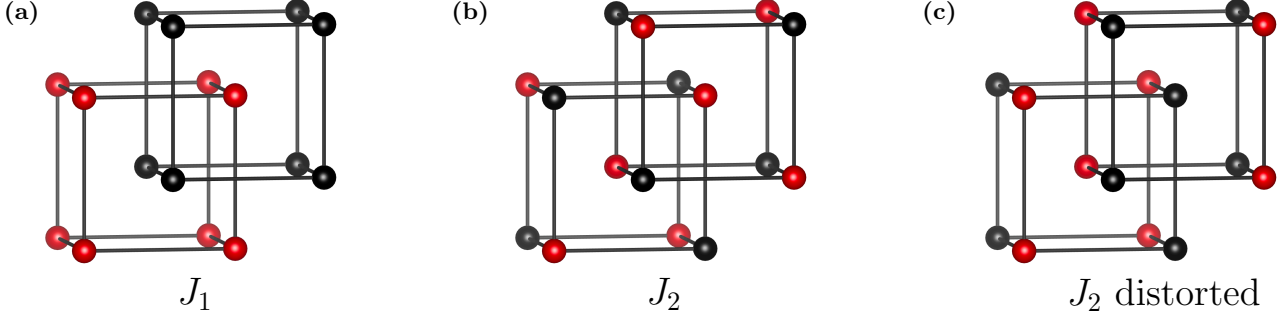


FIG. 6. The sublattices, μ , (red) used to compute the Marshall sign rules defined in Eq. C1. This gives the exact ground-state sign structure for Eq. 1 with (a) $J_1 > 0, J_2 = 0$, (b) $J_1 = 0, J_2 > 0$, and (c) for Eq. 2 with $J_1 = 0, J_{2c} < 0, J_{2ab} > 0$.

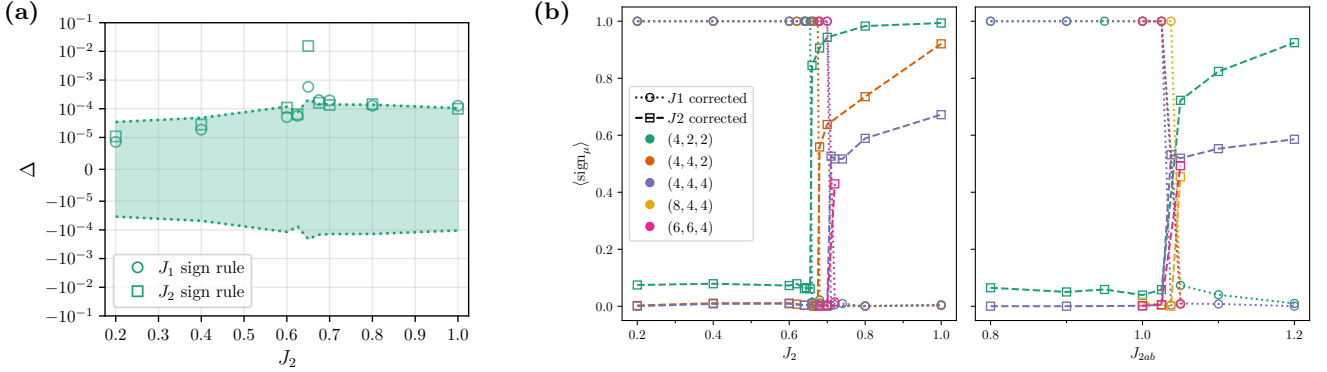


FIG. 7. (a) Variational energies obtained using different sign rules for the $N = 32(4, 2, 2)$ lattice of the cubic-symmetric $J_1 - J_2$ model for different values of J_2 , relative to an ansatz without a sign rule. The shaded regions correspond to the error, due to fluctuations during the final iterations of the optimization. The use of sign rules does not improve variational energies, even for $J_2 \gtrsim 0.65$ where relative errors to the exact solution increase. (b) Expectation values of the Marshall-corrected sign of variational solutions for (left) the cubic $J_1 - J_2$ model and (right) tetragonal $J_1 - J_2$ model.

Appendix E: Tetragonally-distorted $J_1 - J_2 - J_3$ Ising model

Energies for the Néel, collinear and chain phases according to Eq. 6 are

$$\frac{E_{\text{Néel}}}{N} = -4J_1 + J_{2c} + 2J_{2ab} + 4J_{3c} + 2J_{3ab} \quad (\text{E1})$$

$$\frac{E_{\text{collinear}}}{N} = -J_{2c} - 2J_{2ab} + 4J_{3c} + 2J_{3ab} \quad (\text{E2})$$

$$\frac{E_{\text{chain}}}{N} = J_{2c} - 2J_{2ab} - 4J_{3c} + 2J_{3ab}, \quad (\text{E3})$$

such that the Néel and collinear phases are stabilized by a ferromagnetic J_{3c} and the chain phase destabilized. J_{3ab} equally shifts the energy of all phases. Thus the phases have the same energy along $J_{3c} = J_{2c}/4 = 1/2(J_1 - J_{2ab})$. So for ferromagnetic J_{2c} and antiferromagnetic $J_{2ab} < J_1$, a ferromagnetic J_{3c} causes these phases to compete.

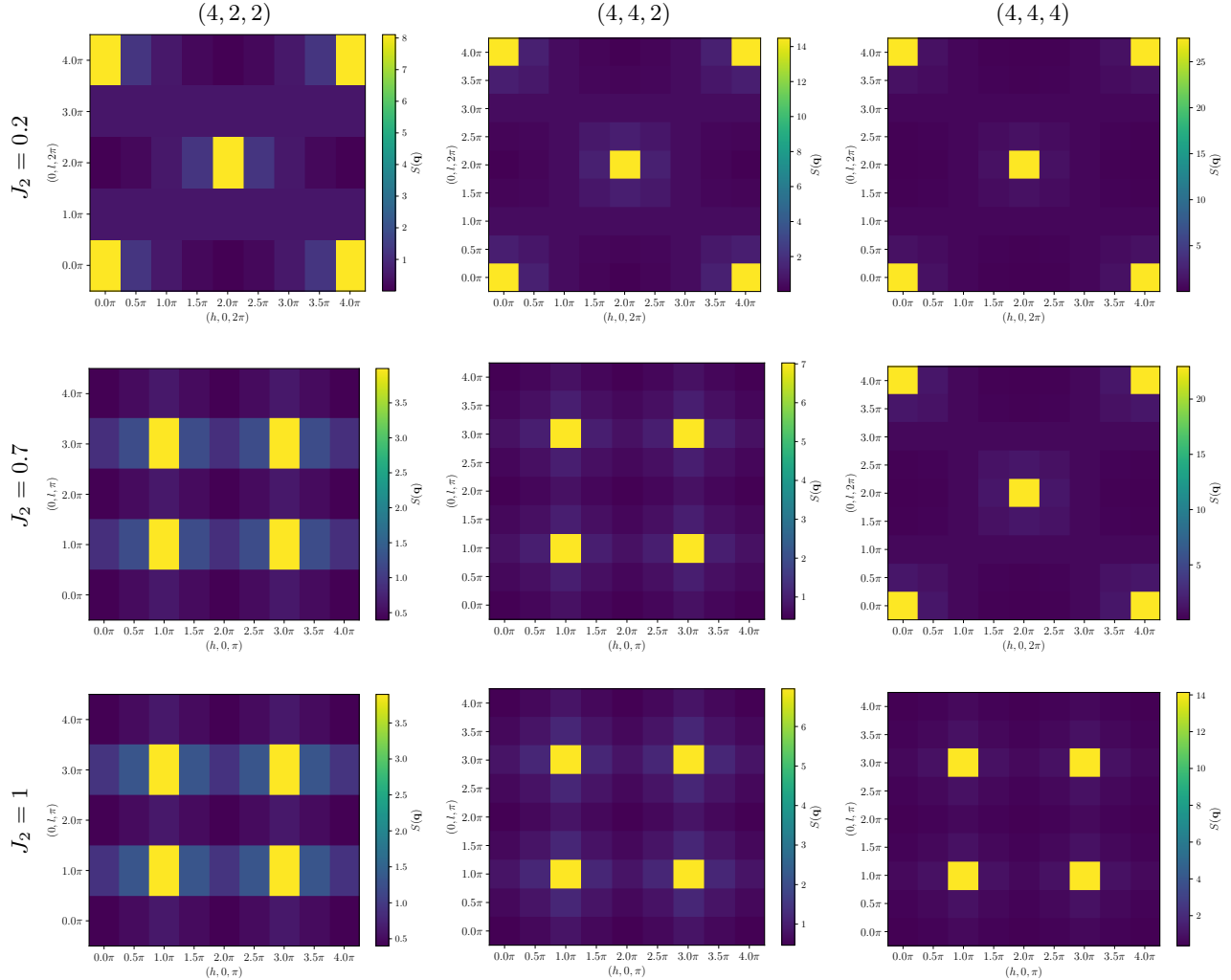


FIG. 8. Ground-state structure factors of the cubic $J_1 - J_2$ model for various J_2 and system sizes, using momentum cuts that show Bragg peaks. Due to the shifting of J_2^c with system size the $(4, 2, 2)$, $(4, 4, 2)$, $J_2 = 0.7$ ground states are in the collinear phase, while for $(4, 4, 4)$, $J_2 = 0.7$ it is in the Néel phase.

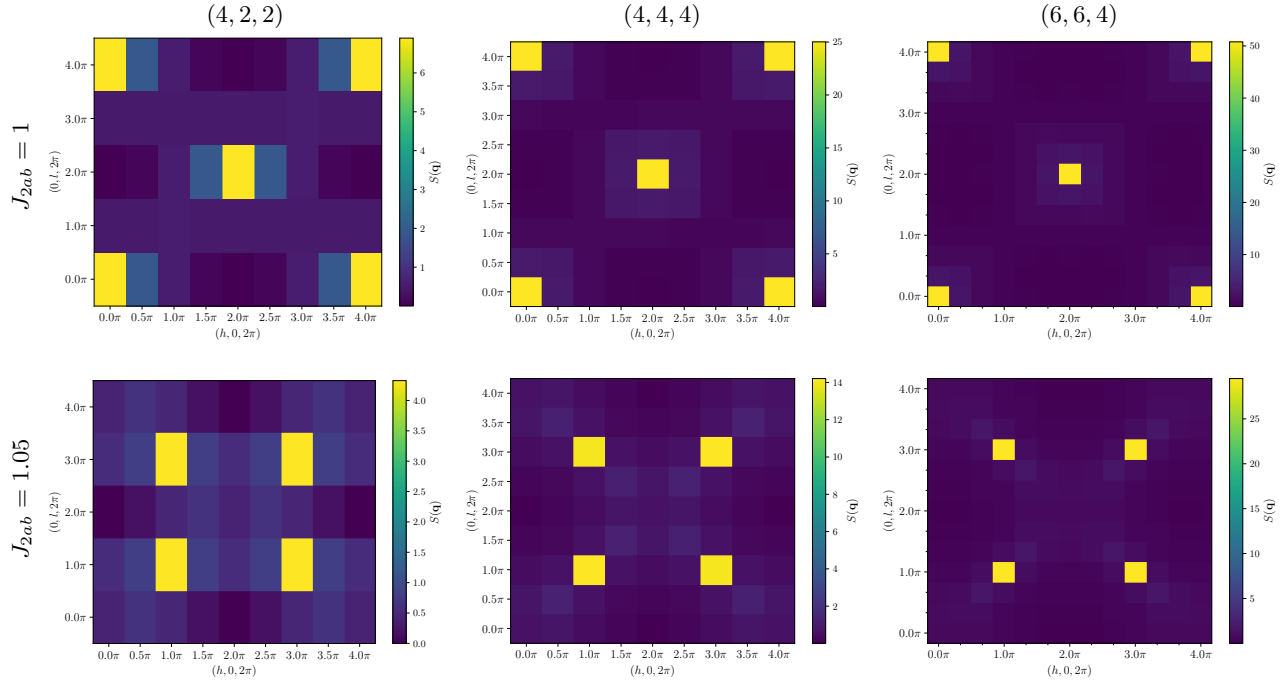


FIG. 9. Ground-state structure factors of the tetragonal model for various J_{2ab} and system sizes in the $(h, l, 2\pi)$ plane.

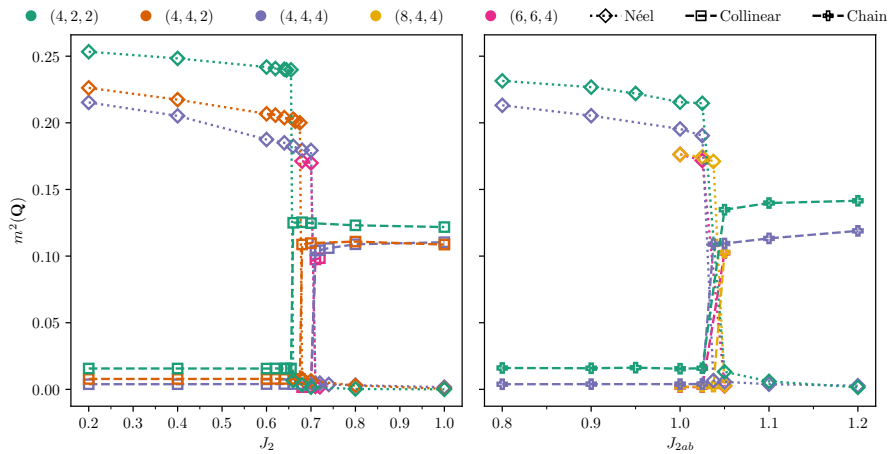


FIG. 10. Ground-state order parameters for the cubic (left) and tetragonal (right) models for different lattice sizes.

[1] C. Lacroix, P. Mendels, and F. Mila, eds., *Introduction to Frustrated Magnetism*, Springer Series in Solid-State Sciences, Vol. 164 (Springer Berlin Heidelberg, Heidelberg, 2011).

[2] Y. Okamoto, M. Nohara, H. Aruga-Katori, and H. Takagi, Spin-Liquid State in the $S = 1/2$ Hyperkagome Antiferromagnet $\text{Na}_4\text{Ir}_3\text{O}_8$, *Physical Review Letters* **99**, 137207 (2007).

[3] S. Chillal, Y. Iqbal, H. O. Jeschke, J. A. Rodriguez-Rivera, R. Bewley, P. Manuel, D. Khalyavin, P. Steffens, R. Thomale, A. T. M. N. Islam, J. Reuther, and B. Lake, Evidence for a three-dimensional quantum spin liquid in $\text{PbCuTe}_2\text{O}_6$, *Nature Communications* **11**, 2348 (2020).

[4] I. Živković, V. Favre, C. Salazar Mejia, H. O. Jeschke, A. Magrez, B. Dabholkar, V. Noculak, R. S. Freitas, M. Jeong, N. G. Hegde, L. Testa, P. Babkevich, Y. Su, P. Manuel, H. Luetkens, C. Baines, P. J. Baker, J. Wosnitza, O. Zaharko, Y. Iqbal, J. Reuther, and H. M. Rønnow, Magnetic Field Induced Quantum Spin Liquid in the Two Coupled Trillium Lattices of $\text{K}_2\text{Ni}_2(\text{SO}_4)_3$, *Physical Review Letters* **127**, 157204 (2021).

[5] J. Khatua, S. Bhattacharya, Q. P. Ding, S. Vrtnik, A. M. Strydom, N. P. Butch, H. Luetkens, E. Kermarrec, M. S. R. Rao, A. Zorko, Y. Furukawa, and P. Khuntia, Spin liquid state in a rare-earth hyperkagome lattice, *Physical Review B* **106**, 104404 (2022).

[6] B. Sana, M. Barik, M. Pregelj, U. Jena, M. Baenitz, J. Sichelschmidt, K. Sethupathi, and P. Khuntia, Magnetic properties of a spin-orbit entangled $J_{\text{eff}} = 1/2$ three-dimensional frustrated rare-earth hyperkagome material, *Physical Review B* **108**, 134413 (2023).

[7] J. G. Rau and M. J. Gingras, Frustrated Quantum Rare-Earth Pyrochlores, *Annual Review of Condensed Matter Physics* **10**, 357 (2019).

[8] R. Sibille, E. Lhotel, V. Pomjakushin, C. Baines, T. Fennell, and M. Kenzelmann, Candidate Quantum Spin Liquid in the $\text{Ce}_3 + \text{Pyrochlore Stannate}$ $\text{Ce}_2\text{Sn}_2\text{O}_7$, *Physical Review Letters* **115**, 097202 (2015).

[9] R. Sibille, N. Gauthier, H. Yan, M. Ciomaga Hanneau, J. Ollivier, B. Winn, U. Filges, G. Balakrishnan, M. Kenzelmann, N. Shannon, and T. Fennell, Experimental signatures of emergent quantum electrodynamics in $\text{Pr}_2\text{Hf}_2\text{O}_7$, *Nature Physics* **14**, 711 (2018).

[10] J. Gaudet, E. M. Smith, J. Dudemaine, J. Beare, C. R. C. Buhariwalla, N. P. Butch, M. B. Stone, A. I. Kolesnikov, G. Xu, D. R. Yahne, K. A. Ross, C. A. Marjerrison, J. D. Garrett, G. M. Luke, A. D. Bianchi, and B. D. Gaulin, Quantum Spin Ice Dynamics in the Dipole-Octupole Pyrochlore Magnet $\text{Ce}_2\text{Zr}_2\text{O}_7$, *Physical Review Letters* **122**, 187201 (2019).

[11] B. Gao, T. Chen, D. W. Tam, C.-L. Huang, K. Sasmal, D. T. Adroja, F. Ye, H. Cao, G. Sala, M. B. Stone, C. Baines, J. A. T. Verezhak, H. Hu, J.-H. Chung, X. Xu, S.-W. Cheong, M. Nallaiyan, S. Spagna, M. B. Maple, A. H. Nevidomskyy, E. Morosan, G. Chen, and P. Dai, Experimental signatures of a three-dimensional quantum spin liquid in effective spin-1/2 $\text{Ce}_2\text{Zr}_2\text{O}_7$ pyrochlore, *Nature Physics* **15**, 1052 (2019).

[12] R. Sibille, N. Gauthier, E. Lhotel, V. Porée, V. Pomjakushin, R. A. Ewings, T. G. Perring, J. Ollivier, A. Wildes, C. Ritter, T. C. Hansen, D. A. Keen, G. J. Nilsen, L. Keller, S. Petit, and T. Fennell, A quantum liquid of magnetic octupoles on the pyrochlore lattice, *Nature Physics* **16**, 546 (2020).

[13] E. M. Smith, O. Benton, D. R. Yahne, B. Placke, R. Schäfer, J. Gaudet, J. Dudemaine, A. Fitterman, J. Beare, A. R. Wildes, S. Bhattacharya, T. DeLazzer, C. R. C. Buhariwalla, N. P. Butch, R. Movshovich, J. D. Garrett, C. A. Marjerrison, J. P. Clancy, E. Kermarrec, G. M. Luke, A. D. Bianchi, K. A. Ross, and B. D. Gaulin, Case for a $U(1)\pi$ Quantum Spin Liquid Ground State in the Dipole-Octupole Pyrochlore $\text{Ce}_2\text{Zr}_2\text{O}_7$, *Physical Review X* **12**, 021015 (2022).

[14] E. M. Smith, E. Lhotel, S. Petit, and B. D. Gaulin, Experimental Insights into Quantum Spin Ice Physics in Dipole-Octupole Pyrochlore Magnets, *Annual Review of Condensed Matter Physics* **16**, 387 (2025).

[15] B. Gao, F. Desrochers, D. W. Tam, D. M. Kirschbaum, P. Steffens, A. Hiess, D. H. Nguyen, Y. Su, S.-W. Cheong, S. Paschen, Y. B. Kim, and P. Dai, Neutron scattering and thermodynamic evidence for emergent photons and fractionalization in a pyrochlore spin ice, *Nature Physics* **21**, 1203 (2025).

[16] J. A. Lussier, B. N. Richtik, C. Mauws, J. W. Lynn, and C. R. Wiebe, Absence of magnetic ordering in the spin liquid candidate $\text{Ca}_3\text{Cu}_2\text{GeV}_2\text{O}_12$, *Journal of Physics: Condensed Matter* **32**, 134001 (2019).

[17] Y. Alexanian, R. Kumar, H. Zeroual, B. Bernu, L. Mangin-Thro, J. R. Stewart, J. M. Wilkinson, S. Bhattacharya, P. L. Paulose, F. Bert, P. Mendels, B. Fåk, and E. Kermarrec, Three-dimensional spin liquid state in the frustrated $\text{SS} = 1/2$ Heisenberg garnet $\text{NaCa}_2\text{Cu}_2(\text{VO}_4)_3$ (2025), arXiv:2501.04653 [cond-mat].

[18] G. Bayer, Vanadates $\text{A}_3\text{B}_2\text{V}_3\text{O}_12$ with Garnet Structure, *Journal of the American Ceramic Society* **48**, 600 (1965).

[19] S. Geller, Crystal Chemistry of the Garnets, *Zeitschrift für Kristallographie* **125**, 1 (1967).

[20] J. Reuther and P. Wölfle, A diagrammatic theory of the antiferromagnetic frustrated 2d Heisenberg model, *Journal of Physics: Conference Series* **200**, 022051 (2010).

[21] J. Reuther and P. Wölfle, $J_1 - J_2$ frustrated two-dimensional Heisenberg model: Random phase approximation and functional renormalization group, *Physical Review B* **81**, 144410 (2010).

[22] N. Niggemann, B. Sbierski, and J. Reuther, Frustrated quantum spins at finite temperature: Pseudo-Majorana functional renormalization group approach, *Physical Review B* **103**, 104431 (2021).

[23] N. Niggemann, J. Reuther, and B. Sbierski, Quantitative functional renormalization for three-dimensional quantum Heisenberg models, *SciPost Physics* **12**, 156 (2022).

[24] T. Müller, D. Kiese, N. Niggemann, B. Sbierski, J. Reuther, S. Trebst, R. Thomale, and Y. Iqbal, Pseudo-fermion functional renormalization group for spin models, *Reports on Progress in Physics* **87**, 036501 (2024).

[25] S. A. Kulagin, N. Prokof'ev, O. A. Starykh, B. Svistunov, and C. N. Varney, Bold Diagrammatic Monte Carlo Method Applied to Fermionized Frustrated Spins, *Physical Review Letters* **110**, 070601 (2013).

[26] S. A. Kulagin, N. Prokof'ev, O. A. Starykh, B. Svistunov, and C. N. Varney, Bold diagrammatic Monte Carlo tech-

nique for frustrated spin systems, *Physical Review B* **87**, 024407 (2013).

[27] Y. Huang, K. Chen, Y. Deng, N. Prokof'ev, and B. Svistunov, Spin-Ice State of the Quantum Heisenberg Antiferromagnet on the Pyrochlore Lattice, *Physical Review Letters* **116**, 177203 (2016).

[28] I. Hagymási, R. Schäfer, R. Moessner, and D. J. Luitz, Magnetization process and ordering of the $S = 1/2$ pyrochlore Heisenberg antiferromagnet in a magnetic field, *Physical Review B* **106**, L060411 (2022).

[29] D. Tahara and M. Imada, Variational Monte Carlo Method Combined with Quantum-Number Projection and Multi-Variable Optimization, *Journal of the Physical Society of Japan* **77**, 114701 (2008).

[30] N. Astrakhantsev, T. Westerhout, A. Tiwari, K. Choo, A. Chen, M. H. Fischer, G. Carleo, and T. Neupert, Broken-Symmetry Ground States of the Heisenberg Model on the Pyrochlore Lattice, *Physical Review X* **11**, 041021 (2021).

[31] R. Pohle, Y. Yamaji, and M. Imada, Ground state of the $S=1/2$ pyrochlore Heisenberg antiferromagnet: A quantum spin liquid emergent from dimensional reduction (2023), arXiv:2311.11561 [cond-mat, physics:quant-ph].

[32] R. F. Bishop, D. J. J. Farnell, and J. B. Parkinson, Phase transitions in the spin-half $J_1 - J_2$ model, *Physical Review B* **58**, 6394 (1998).

[33] M. P. Gelfand and R. R. P. Singh, High-order convergent expansions for quantum many particle systems, *Advances in Physics* **49**, 93 (2000).

[34] C. Roth, A. Szabó, and A. H. MacDonald, High-accuracy variational Monte Carlo for frustrated magnets with deep neural networks, *Physical Review B* **108**, 054410 (2023).

[35] A. Chen, Empowering deep neural quantum states through efficient optimization, *Nature Physics* (2024).

[36] R. Rende, L. L. Viteritti, L. Bardone, F. Becca, and S. Goldt, A simple linear algebra identity to optimize large-scale neural network quantum states, *Communications Physics* **7**, 260 (2024).

[37] L. L. Viteritti, R. Rende, A. Parola, S. Goldt, and F. Becca, Transformer wave function for two dimensional frustrated magnets: Emergence of a spin-liquid phase in the Shastry-Sutherland model, *Physical Review B* **111**, 134411 (2025).

[38] T. Duric, J. H. Chung, B. Yang, and P. Sengupta, Spin-1 / 2 Kagome Heisenberg Antiferromagnet: Machine Learning Discovery of the Spinon Pair-Density-Wave Ground State, *Physical Review X* **15**, 011047 (2025).

[39] R. Schmidt, J. Schulenburg, J. Richter, and D. D. Betts, Spin-1/2 $J_1 - J_2$ model on the body-centered cubic lattice, *Physical Review B* **66**, 224406 (2002).

[40] J. Oitmaa and W. Zheng, Phase diagram of the bcc $S = 1/2$ Heisenberg antiferromagnet with first and second neighbor exchange, *Physical Review B* **69**, 064416 (2004).

[41] K. Majumdar and T. Datta, Non-linear spin wave theory results for the frustrated $S=\sqrt{1/2}$ Heisenberg antiferromagnet on a body-centered cubic lattice, *Journal of Physics: Condensed Matter* **21**, 406004 (2009).

[42] M. R. Pantić, D. V. Kapor, S. M. Radošević, and P. M. Mali, Phase diagram of spin-12 quantum Heisenberg $J_1 - J_2$ antiferromagnet on the body-centered-cubic lattice in random phase approximation, *Solid State Communications* **182**, 55 (2014).

[43] D. J. J. Farnell, O. Götze, and J. Richter, Ground-state ordering of the $J_1 - J_2$ model on the simple cubic and body-centered cubic lattices, *Physical Review B* **93**, 235123 (2016).

[44] P. Ghosh, T. Müller, F. P. Toldin, J. Richter, R. Narayanan, R. Thomale, J. Reuther, and Y. Iqbal, Quantum paramagnetism and helimagnetic orders in the Heisenberg model on the body centered cubic lattice, *Physical Review B* **100**, 014420 (2019).

[45] L. L. Viteritti, R. Rende, and F. Becca, Transformer Variational Wave Functions for Frustrated Quantum Spin Systems, *Physical Review Letters* **130**, 236401 (2023).

[46] R. P. Nutakki, A. Shokry, and F. Vicentini, Design principles of deep translationally symmetric neural quantum states for frustrated magnets, *Physical Review Research* **7**, 043099 (2025).

[47] S. Morita, R. Kaneko, and M. Imada, Quantum Spin Liquid in Spin 1/2 $J_1 - J_2$ Heisenberg Model on Square Lattice: Many-Variable Variational Monte Carlo Study Combined with Quantum-Number Projections, *Journal of the Physical Society of Japan* **84**, 024720 (2015).

[48] Y. Nomura, Helping restricted Boltzmann machines with quantum-state representation by restoring symmetry, *Journal of Physics: Condensed Matter* **33**, 174003 (2021).

[49] R. K. Kaul, Spin Nematics, Valence-Bond Solids, and Spin Liquids in SO (N) Quantum Spin Models on the Triangular Lattice, *Physical Review Letters* **115**, 157202 (2015).

[50] S. Pujari, T. C. Lang, G. Murthy, and R. K. Kaul, Interaction-Induced Dirac Fermions from Quadratic Band Touching in Bilayer Graphene, *Physical Review Letters* **117**, 086404 (2016).

[51] Y. Nomura and M. Imada, Dirac-Type Nodal Spin Liquid Revealed by Refined Quantum Many-Body Solver Using Neural-Network Wave Function, Correlation Ratio, and Level Spectroscopy, *Physical Review X* **11**, 031034 (2021).

[52] T. Westerhout, N. Astrakhantsev, K. S. Tikhonov, M. I. Katsnelson, and A. A. Bagrov, Generalization properties of neural network approximations to frustrated magnet ground states, *Nature Communications* **11**, 1593 (2020).

[53] I. Schurov, A. Kravchenko, M. I. Katsnelson, A. A. Bagrov, and T. Westerhout, Learning complexity of many-body quantum sign structures through the lens of Boolean Fourier analysis (2025), arXiv:2508.09870 [cond-mat].

[54] R. P. Nutakki and F. Vicentini, Data for “Ground-state phases of $S=1/2$ Heisenberg models on the body-centered cubic lattice”, 10.5281/zenodo.18592704 (2026).

[55] Neural quantum states for the body-centered cubic lattice, <https://github.com/NeuralQXLab/bcc-nqs> (2026).

[56] M. Reh, M. Schmitt, and M. Gärttner, Optimizing design choices for neural quantum states, *Physical Review B* **107**, 195115 (2023).

[57] W. Marshall, Antiferromagnetism, *Proceedings of the Royal Society of London. A. Mathematical and Physical Sciences* **232**, 48 (1955).

[58] M. S. Moss, R. Wiersema, M. Hibat-Allah, J. Carrasquilla, and R. G. Melko, Leveraging recurrence in neural network wavefunctions for large-scale simulations of Heisenberg antiferromagnets: The square lattice (2025), arXiv:2502.17144 [cond-mat].

[59] A. Szabó and C. Castelnovo, Neural network wave functions and the sign problem, *Physical Review Research* **2**,

033075 (2020).